Dynamic Modeling and Performance Analysis of a New Redundant Parallel Rehabilitation Robot

SHENGLONG XIE[ID]1, KAIMING HU1, HAITAO LIU2, (Member, IEEE), AND YANJIAN WAN1
1School of Mechanical and Electrical Engineering, China Jiliang University, Hangzhou 310018, China
2Key Laboratory of Mechanism Theory and Equipment Design of Ministry of Education, Tianjin University, Tianjin 300354, China

Corresponding author: Haitao Liu (liuht@tju.edu.cn)

ABSTRACT The inverse dynamic model and performance analysis of a new redundant parallel rehabilitation robot are presented in this paper. First, the kinematics of each part is analyzed based on a closed-loop vector chain method. Then, the dynamic model of each part is formulated based on the D'Alembert principle and Euler's equation. After that, the inverse dynamic formulation of the new redundant parallel robot is established by utilizing the principle of virtual work and the concept of linked Jacobian matrices. To validate the approach, dynamic simulations are implemented in ADAMS and MATLAB. The results demonstrate the correctness of this dynamic formulation. Then, the actuating forces are optimized by utilizing the weighted Moore-Penrose generalized inverse method, which determines the minimum norm of the least quadratic sum among the possible actuating force vectors. Finally, two novel dynamic performance indices are defined. The first index reflects the coupling effect of other neighboring limbs to the dominant limb; the second reflects the coupling effect of each neighboring limb to the dominant limb. The proposed approach can be used for the dynamic performance analysis in other types of redundant parallel robots and provides a reference for dynamic control strategies.

INDEX TERMS Inverse dynamics, redundant parallel robot, rehabilitation robot, performance analysis, virtual work.

I. INTRODUCTION

With the global escalation of aging populations, the lower limb dyskinesia case caused by strokes, spinal cord and brain injuries has increased in recent years. In order to reach the requirements of high frequency, high intensity, strong pertinence, repetition, and continuity for rehabilitation training, the lower limb rehabilitation robot has become a research hotspot.

Generally speaking, the lower limb rehabilitation robot has two configurations: the parallel and the series. Compared with a serial robot, a parallel robot is a closed-loop mechanism whose moving platform is connected with a fixed base by several independent kinematic branches [1]. This structure makes it has several advantages, including larger payload capacity [2], higher mechanical stiffness, and faster response [3] (or wider bandwidth). So, it has been widely applied in medical rehabilitation robots. However, parallel robots also suffer from disadvantages including singularities, low dexterities, and small workspaces [4]. Redundancy is

The associate editor coordinating the review of this manuscript and approving it for publication was Guilin Yang[ID].

considered as an alternative way to conquer these disadvantages by improving the performance and capability of parallel robots. The redundancy can increase the workspace [5], reduce or even eliminate the kinematic singularities [6], improve dexterity, and eliminate force-unconstrained configurations [7]. The redundant robot is a parallel robot whose actuators exceed the total degrees-of-freedom (DOF) required for the task [8]. Redundancy in a parallel robot can be divided into three categories [9]: (1) kinematic redundancy, which adds additional active joints in one or more branches than required. This increases the workspace and avoids most singular configurations effectively, while increasing the complexity of kinematic analyses. (2) actuation redundancy. This has two types [10], namely 'in-branch redundancy' and 'branch redundancy'. The former one replaces one or more of the passive joints with active ones without changing the kinematic architecture. The later one adds at least one extra branch with an active joint. (3) combined redundancy, which is a combination of the two above.

As the number of drives is greater than the DOF of the redundant derived mechanism, the coordination between the

various drives of the mechanism is required to be higher. The traditional position control method has been unable to meet the control performance requirements. In order to achieve a better therapeutic effect, the force control is proposed. It can be divided into hybrid force/position control and impedance control [11]. Both of the two control strategies need the dynamic model of a robot in most cases. Meanwhile, the dynamic model can provide the essential mathematical model to research the dynamic characteristics of robots and determine the parameters of drivers, like rated speed, torque, and power [12]. So, it is very important to determine the dynamic equation of a robot [13]. There are several approaches to develop the dynamic equation of a parallel robot. They can be classified into five categories: (1) Newton–Euler method [14], which is based on the balance of forces/moments and is more suitable for serial robot [15]. (2) Kane's method [16], which derives the dynamic equations based on the partial velocities of the constituents of the system [17]. (3) Lagrange method [18], which formulates dynamic equations of motion by using Lagrangian functions and can be expressed in closed form [19]. (4) virtual work principle method [20], which develops dynamic equations by using D'Alembert principle to formulate the equilibrium equations; this category assumes the work performed by the external forces through virtual displacements compatible with the system is zero. (5) Gibbs-Appell formulation [21], which is derived from Gibbs equation (acceleration energy equation). It can separate some dynamic parameters from the model very well and has the merits of deriving motion equations of closed-chain robotic system. The Newton–Euler method usually requires a large computation time, since it needs the detailed calculations of all internal constrained reactions of the system, even if they are not used in the dynamic analysis or the control strategy of the robot [22]. The Kane's method needs to calculate accelerations, partial velocities of mass centers, and partial angular velocities of all links, which is computationally expensive. The Lagrangian method needs to compute large amounts of symbolic partial derivatives, and it may contain some unknown constraint forces in Lagrangian multipliers when non-independent generalized variables are introduced. This method requires solving the kinematic constraint equations and leads to additional computations. The virtual work principle method is an efficient approach for the dynamic modeling of the parallel robot [23]. Its advantages include less redundant information, concise representations, and high computational efficiency [24].

Meanwhile, the force control strategies based on joint space result in a deterioration of performance for the different DOF that possess significant coupling in parallel robots [25]. The inertia property is a direct reflection of coupling, and are key parameters to determine the drive system. So, the inertia property is of great significance for dynamic performance analysis, design, and control [26]; it has attracted the extensive attention of researchers. Yao [27] researches the block diagonal dominant property of the Stewart robot based on the inertia matrix in joint-space to indicate the coupling effect of

neighboring limbs. While Ogbobe [28] analyzes the coupling effects between the DOF of the Stewart parallel robot based on the joint-space mass matrix. Wang [29] proposes an inertia coupling index based on the inertia matrix of 3-PRS parallel robot and analyses the distribution of the index in workspace; this work is validated by experiment. Shao [30] proposes an inertia index, namely the Joint-Reflected Inertia (JRI), and investigates the inertia matching method by taking the Stewart parallel robot as a study object. After that, Mo [26] proposes the joint-space Inertia (CVI) index to address a limitation of the JRI: it fails to reflect the imbalance of the inertia property among limbs. Zhao [31] presents a novel dynamic performance index that has combined the acceleration, velocity, and gravity terms to analyze the dynamic performance in different directions of a redundant parallel robot. Meanwhile, he adopts a series of kinematics and dynamic performance indices to compare the performance of the 8PSS redundant parallel robot to that of the 6PSS parallel robot. The author concludes the dynamic performance of the 8PSS redundant parallel robot is better than the 6PSS [32]. After that, the research on the dynamic performance of redundant parallel robot seems to have no substantial improvement. In fact, the Jacobi matrix of a redundant parallel robot is not a square matrix anymore, since the actuator redundancy establishes an over-constrained mechanism. This yields the generalized inertia matrix which describes the mapping between the actuating forces/torques and the accelerations is not a square matrix [32]. As a result, the conditioning indices cannot be used in the redundant parallel robot directly. Actually, the work on the dynamic performance analysis of the redundant parallel robot is sparse. Meanwhile, previous research has failed to analyze the coupling effects of redundant parallel robots, and the inertia index cannot reflect the coupling effect of each neighboring limb to the dominant limb. Therefore, this paper is dedicated to analyzing the coupling effects of redundant parallel robots and revealing the coupling effect of each neighboring limb to the dominant limb by introducing two dynamic indices. To this end, the inverse dynamic model of a novel redundant parallel robot actuated with pneumatic artificial muscles is established using the virtual work principle.

The rest of this paper is organized as follows. Firstly, the architecture of this new robot is introduced briefly, and the kinematics of each part is analyzed. Secondly, the dynamic model of each part is formulated based on the D'Alembert principle and Euler's equation. After that, the inverse dynamic formulation of the new redundant parallel robot is established based on the principle of virtual work [33] and the concept of link Jacobian matrices [34]. Then, the numeric simulation is implemented in both ADAMS and MATLAB to validate the correctness of the inverse dynamic formulation. Subsequently, the actuating forces of each driving limb are optimized by using the weighted Moore-Penrose generalized inverse method. Finally, two novel dynamic performance indices are defined to reflect the coupling effect of other neighboring limbs to the dominant limb and the coupling
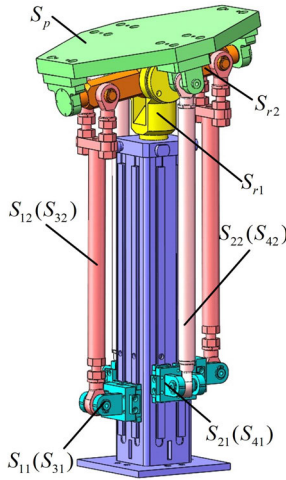
FIGURE 1. Main part of AirGait.

effect of each neighboring limb to the dominant limb, respectively.

II. KINEMATIC ANALYSIS

The kinematic analysis and Jacobian analysis of the proposed robot are performed in this section.

A. SYSTEM DESCRIPTION

Fig. 1 illustrates the virtual prototype of our study object, which is the main part of a new parallel rehabilitant robot-AirGait [35]. It contains two bodies (the moving platform and the base), PRR limbs, PSS limbs, and PR limbs (also called restricted limbs). The topological structure is a 3-DOF 2-PSS-(2-PRR-PR) R parallel mechanism. Here, R, P, and S denote revolute, prismatic, and spherical joints, respectively; P denotes an actuated prismatic joint. Limb 1 and 2 belong to the PRR limb, while limb 3 and 4 belong to the PSS limb. Both of the PRR limbs and PSS limbs can be divided into part S_{i1} (consisting of slide block and accessories) and S_{i2} (moving limb), and the PR limbs contain part S_{r1} (P limb) and S_{r2} (R limb). With the notable structure, the mechanism possesses 3 DOF, including one translation along the vertical direction and one rotation about axis v (called the dorsal/plantar flexion movement) and one rotation about axis u (called the inversion/extroversion movement).

Fig. 2 shows the kinematic diagram of AirGait, where $B_i(i = 1, 2, 3, 4)$ is the intersection point of the prismatic joint and the base; A_1, A_3, P_1, and P_3 are the centers of revolute joints of the PRR limbs; A_2, A_4, P_2, and P_4 are the centers of the spherical joints of PSS limbs; O and O' are the centers of the base and moving platform, respectively. Coordinate $O - xyz$ (called $\mathcal{K}$ for simplicity) is established in point O with the axis x along the vector OB_1, the axis z is vertical to the plane consisting of point $B_i(i = 1, 2, 3, 4)$, and the axis y obeys right-hand rule. θ is the rotation angle of the moving platform around the axis v (called the dorsal/plantar flexion angle) and ψ is the rotation angle of the moving platform around the axis u (called the inversion/extroversion angle).

Fig. 3 shows the schematic diagram of the moving platform. The local coordinate $O'-uvw$ (called $\mathcal{K}'$ for simplicity)
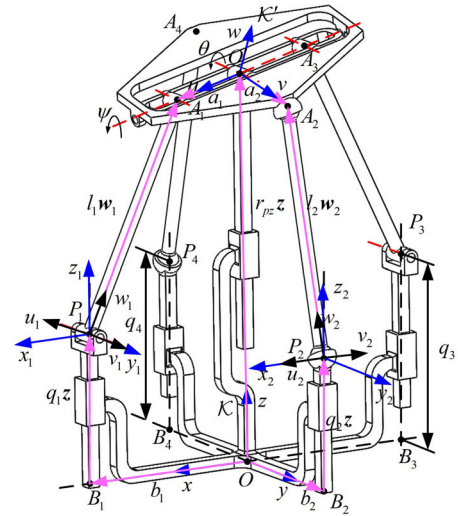

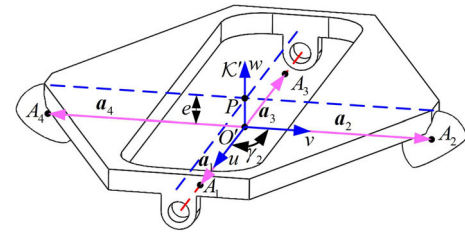**FIGURE 2.** Kinematic diagram of AirGait.

FIGURE 3. Scheme diagram of the moving platform.

is established in point O' to describe the position and orientation of the moving platform. Here, the axis u points from O' to A_1, the axis w is vertical to the plan consist of point $A_i(i = 1, 2, 3, 4)$, and the axis v obeys the right-hand rule. Then, the orientation matrix of $\mathcal{K}'$ relative to $\mathcal{K}$ can be expressed as

$$
\begin{aligned}
\boldsymbol{R} &= \text{Rot}(y, \theta)\,\text{Rot}(u, \psi) \\
&= \begin{bmatrix}
\cos\theta & \sin\psi\sin\theta & \cos\psi\sin\theta \\
0 & \cos\psi & -\sin\psi \\
-\sin\theta & \sin\psi\cos\theta & \cos\psi\cos\theta
\end{bmatrix} \\
&= \begin{bmatrix} \boldsymbol{u} & \boldsymbol{v} & \boldsymbol{w} \end{bmatrix}
\end{aligned}
\tag{1}
$$

where $\boldsymbol{u}$, $\boldsymbol{v}$ and $\boldsymbol{w}$ represent the unit vectors of the u-, v- and w-axis, respectively.

In addition, e is the distance between point P and O', γ_i is the angle of $\overline{OB_i}$ relative to the axis x (or $\overline{PA_i}$ relative to the axis u), and

$$
\gamma_i = (i-1)\frac{\pi}{2}, \quad i = 1, 2, 3, 4. \tag{2}
$$

B. INVERSE KINEMATICS

The closed-loop vector equation of O' which associated with the ith kinematic chain is as follows

$$
\boldsymbol{r} = \boldsymbol{b}_i + q_i\boldsymbol{z} + l_i\boldsymbol{w}_i - \boldsymbol{a}_i, \quad i = 1, 2, 3, 4 \tag{3}
$$

where $\boldsymbol{r}, \boldsymbol{a}_i, \boldsymbol{b}_i, q_i, l_i$ denote the vector OO', the vector OA_i, the vector OB_i, the ith active joint variable, and the length

of P_iA_i, respectively; z denotes the unit vector of the axis z and w_i denotes the unit vector along P_iA_i.

$$\boldsymbol{b}_i = b_i \begin{pmatrix} \cos\gamma_i & \sin\gamma_i & 0 \end{pmatrix}^{\mathrm{T}},$$

$$\boldsymbol{a}_{i0} = a_i \begin{pmatrix} \cos\gamma_i & \sin\gamma_i & 0 \end{pmatrix}^{\mathrm{T}},$$

$$b_1 = b_3, \quad b_2 = b_4, \quad a_1 = a_3, \quad a_2 = a_4, \quad l_1 = l_3, \quad l_2 = l_4$$

where a_i and b_i are the length of OA_i and OB_i, respectively.

By assuming $\boldsymbol{c}_i = \boldsymbol{a}_i - \boldsymbol{b}_i$, Eq. (3) can be expressed as

$$r_z z + \boldsymbol{c}_i - q_i z = l_i \boldsymbol{w}_i, \quad i = 1, 2, 3, 4 \tag{4}$$

where r_z is the length of $O'O$.

Then, the inverse position solution can be achieved as follows

$$q_i = (\boldsymbol{c}_i^{\mathrm{T}} z + r_z) - \sqrt{l_i^2 - ((\boldsymbol{c}_i^{\mathrm{T}} \boldsymbol{x})^2 + (\boldsymbol{c}_i^{\mathrm{T}} \boldsymbol{y})^2)}, \quad i = 1, 2, 3, 4 \tag{5}$$

where $\boldsymbol{x}$ denotes the unit vector of the axis x, $\boldsymbol{y}$ denotes the unit vector of the axis y.

Meanwhile, we can obtain the unit vector of each chain according to Eq. (3) as follows

$$\boldsymbol{w}_i = (\boldsymbol{r} - \boldsymbol{b}_i - q_i z + \boldsymbol{a}_i)/l_i, \quad i = 1, 2, 3, 4. \tag{6}$$

C. VELOCITY ANALYSIS

Taking the differentiation of Eq. (3) with respect to time yields

$$\dot{r}_z z = \dot{q}_i z + l_i \boldsymbol{\omega}_i \times \boldsymbol{w}_i - \boldsymbol{\omega} \times \boldsymbol{a}_i \tag{7}$$

where $\boldsymbol{\omega}_i$ and $\boldsymbol{\omega}$ are the angular velocity of the ith limb and the moving platform, respectively.

Taking the dot product with $\boldsymbol{w}_i^{\mathrm{T}}$ on both sides of Eq. (7) leads to

$$\boldsymbol{w}_i^{\mathrm{T}} z \dot{q}_i = \boldsymbol{w}_i^{\mathrm{T}} z \dot{r}_z + (\boldsymbol{a}_i \times \boldsymbol{w}_i)^{\mathrm{T}} \boldsymbol{\omega}. \tag{8}$$

Substituting $\boldsymbol{\omega} = \dot{\theta} \boldsymbol{y} + \dot{\psi} \boldsymbol{u}$ into Eq. (8) yields

$$\dot{q}_i = \dot{r}_z + w_{iz}^{-1} (\boldsymbol{a}_i \times \boldsymbol{w}_i)^{\mathrm{T}} \boldsymbol{y} \dot{\theta} + w_{iz}^{-1} (\boldsymbol{a}_i \times \boldsymbol{w}_i)^{\mathrm{T}} \boldsymbol{u} \dot{\psi} \tag{9}$$

where

$$w_{iz}^{-1} = \frac{1}{w_{iz}} = \frac{1}{\boldsymbol{w}_i^{\mathrm{T}} z}$$

Introducing r_z, θ, and ψ as an independent generalized coordinate $\boldsymbol{\Theta}$, namely $\boldsymbol{\Theta} = \begin{bmatrix} r_z & \theta & \psi \end{bmatrix}^{\mathrm{T}}$, then Eq. (9) can be rewritten in the matrix form

$$\dot{\boldsymbol{q}} = \boldsymbol{J} \dot{\boldsymbol{\Theta}} \tag{10}$$

where

$$\dot{\boldsymbol{q}} = \begin{pmatrix} \dot{q}_1 \\ \dot{q}_2 \\ \dot{q}_3 \\ \dot{q}_4 \end{pmatrix},$$

$$\boldsymbol{J} = \begin{bmatrix} 1 & w_{1z}^{-1} (\boldsymbol{a}_1 \times \boldsymbol{w}_1)^{\mathrm{T}} \boldsymbol{y} & w_{1z}^{-1} (\boldsymbol{a}_1 \times \boldsymbol{w}_1)^{\mathrm{T}} \boldsymbol{u} \\ 1 & w_{2z}^{-1} (\boldsymbol{a}_2 \times \boldsymbol{w}_2)^{\mathrm{T}} \boldsymbol{y} & w_{2z}^{-1} (\boldsymbol{a}_2 \times \boldsymbol{w}_2)^{\mathrm{T}} \boldsymbol{u} \\ 1 & w_{3z}^{-1} (\boldsymbol{a}_3 \times \boldsymbol{w}_3)^{\mathrm{T}} \boldsymbol{y} & w_{3z}^{-1} (\boldsymbol{a}_3 \times \boldsymbol{w}_3)^{\mathrm{T}} \boldsymbol{u} \\ 1 & w_{4z}^{-1} (\boldsymbol{a}_4 \times \boldsymbol{w}_4)^{\mathrm{T}} \boldsymbol{y} & w_{4z}^{-1} (\boldsymbol{a}_4 \times \boldsymbol{w}_4)^{\mathrm{T}} \boldsymbol{u} \end{bmatrix}$$

$$\dot{\boldsymbol{\Theta}} = \begin{bmatrix} \dot{r}_z & \dot{\theta} & \dot{\psi} \end{bmatrix}^{\mathrm{T}}.$$

Taking the dot product z on both sides of Eq. (9) leads to

$$\dot{\boldsymbol{q}}_i = \dot{r}_z z + w_{iz}^{-1} z (\boldsymbol{a}_i \times \boldsymbol{w}_i)^{\mathrm{T}} \boldsymbol{y} \dot{\theta} + w_{iz}^{-1} z (\boldsymbol{a}_i \times \boldsymbol{w}_i)^{\mathrm{T}} \boldsymbol{u} \dot{\psi} \tag{11}$$

where

$$\dot{\boldsymbol{q}}_i = \dot{q}_i z = \begin{pmatrix} 0 & 0 & \dot{q}_i \end{pmatrix}^{\mathrm{T}}.$$

Rewriting Eq. (11) in the matrix form yields

$$\dot{\boldsymbol{q}}_i = \boldsymbol{J}_{qi} \dot{\boldsymbol{\Theta}} \tag{12}$$

where

$$\boldsymbol{J}_{qi} = \begin{bmatrix} z & w_{iz}^{-1} z (\boldsymbol{a}_i \times \boldsymbol{w}_i)^{\mathrm{T}} \boldsymbol{y} & w_{iz}^{-1} z (\boldsymbol{a}_i \times \boldsymbol{w}_i)^{\mathrm{T}} \boldsymbol{u} \end{bmatrix}.$$

D. ACCELERATION ANALYSIS

Taking the differentiation of Eq. (10) with respect to time gives

$$\ddot{\boldsymbol{q}} = \dot{\boldsymbol{J}} \dot{\boldsymbol{\Theta}} + \boldsymbol{J} \ddot{\boldsymbol{\Theta}} \tag{13}$$

where

$$\ddot{\boldsymbol{q}} = \begin{bmatrix} \ddot{q}_1 & \ddot{q}_2 & \ddot{q}_3 & \ddot{q}_4 \end{bmatrix}^{\mathrm{T}}, \quad \dot{\boldsymbol{J}}_i = \begin{bmatrix} 0 & \dot{J}_{i1} & \dot{J}_{i2} \end{bmatrix}$$

$$\ddot{\boldsymbol{\Theta}} = \begin{bmatrix} \ddot{r}_z & \ddot{\theta} & \ddot{\psi} \end{bmatrix}^{\mathrm{T}}$$

$$\dot{J}_{i1} = \frac{(\boldsymbol{\omega}_i \times \boldsymbol{w}_i)^{\mathrm{T}} z (\boldsymbol{a}_i \times \boldsymbol{w}_i)^{\mathrm{T}} \boldsymbol{y} - (\boldsymbol{w}_i^{\mathrm{T}} z) \boldsymbol{J}_{pyi} \boldsymbol{y}}{(\boldsymbol{w}_i^{\mathrm{T}} z)^2}$$

$$\dot{J}_{i2} = \frac{(\boldsymbol{\omega}_i \times \boldsymbol{w}_i)^{\mathrm{T}} z (\boldsymbol{a}_i \times \boldsymbol{w}_i)^{\mathrm{T}} \boldsymbol{u} - (\boldsymbol{w}_i^{\mathrm{T}} z) (\boldsymbol{J}_{pyi} \boldsymbol{u} + \boldsymbol{J}_{pui} \dot{\boldsymbol{u}})}{(\boldsymbol{w}_i^{\mathrm{T}} z)^2}.$$

Taking the differentiation of Eq. (12) with respect to time gives

$$\ddot{\boldsymbol{q}}_i = \dot{\boldsymbol{J}}_{qi} \dot{\boldsymbol{\Theta}} + \boldsymbol{J}_{qi} \ddot{\boldsymbol{\Theta}} \tag{14}$$

where

$$\dot{\boldsymbol{J}}_{qi} = \begin{bmatrix} \dot{J}_{qi1} & \dot{J}_{qi2} & \dot{J}_{qi3} \end{bmatrix}, \quad \dot{J}_{qi1} = \boldsymbol{0},$$

$$\dot{J}_{qi2} = \left(\frac{(\boldsymbol{\omega}_i \times \boldsymbol{w}_i)^{\mathrm{T}} zz (\boldsymbol{a}_i \times \boldsymbol{w}_i)^{\mathrm{T}} \boldsymbol{y} - \boldsymbol{w}_i^{\mathrm{T}} zz \boldsymbol{J}_{pyi} \boldsymbol{y}}{(\boldsymbol{w}_i^{\mathrm{T}} z)^2} \right),$$

$$\dot{J}_{qi3} = \left(\frac{(\boldsymbol{\omega}_i \times \boldsymbol{w}_i)^{\mathrm{T}} zz (\boldsymbol{a}_i \times \boldsymbol{w}_i)^{\mathrm{T}} \boldsymbol{u} - \boldsymbol{w}_i^{\mathrm{T}} zz (\boldsymbol{J}_{pyi} \boldsymbol{u} + \boldsymbol{J}_{pui} \dot{\boldsymbol{u}})}{(\boldsymbol{w}_i^{\mathrm{T}} z)^2} \right),$$

$$\dot{\boldsymbol{u}} = \begin{bmatrix} -\sin\theta & 0 & -\cos\theta \end{bmatrix}^{\mathrm{T}},$$

$$\boldsymbol{J}_{pyi} = \left((\boldsymbol{a}_i^{\mathrm{T}} \boldsymbol{w}_i \boldsymbol{E}_3 - \boldsymbol{w}_i \boldsymbol{a}_i^{\mathrm{T}}) \boldsymbol{\omega}_i + (\boldsymbol{a}_i \boldsymbol{w}_i^{\mathrm{T}} - \boldsymbol{w}_i^{\mathrm{T}} \boldsymbol{a}_i \boldsymbol{E}_3) \boldsymbol{\omega} \right)^{\mathrm{T}},$$

$$\boldsymbol{J}_{pui} = (\boldsymbol{a}_i \times \boldsymbol{w}_i)^{\mathrm{T}}.$$

III. DYNAMIC ANALYSIS

Fig. 4 illustrates the modeling process of the inverse dynamic model for the proposed parallel robot. Firstly, the kinematics of each part of this robot is analyzed. Then, the dynamic model of each part is established based on the D'Alembert principle and Euler's equation. Finally, the inverse dynamic equation of this robot is formulated by utilizing the principle of virtual work.
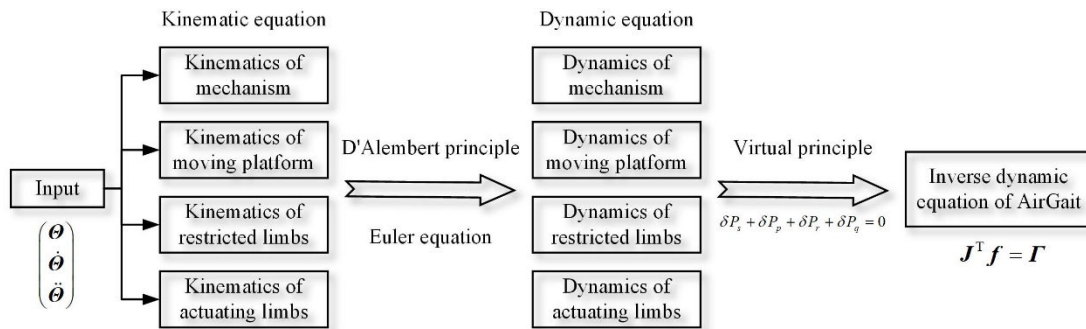
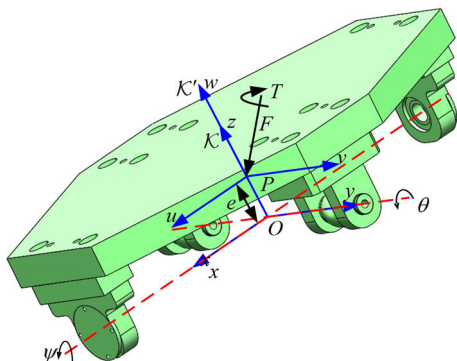FIGURE 4. The modeling process of inverse dynamic model.

FIGURE 5. Moving platform.

A. SUBSYSTEM KINEMATIC ANALYSIS
1) KINEMATICS OF MOVING PLATFORM

Fig. 5 illustrates the kinematic parameters and the free-body diagram of the moving platform.

$$\dot{r}_p = \dot{r} + \omega \times e \quad (15)$$

where $\dot{r}_p$ is the velocity of point P and ω is the angular velocity of the moving platform.

The angular velocity of the moving platform is

$$\omega = \dot{\theta} y + \dot{\psi} u. \quad (16)$$

Substituting Eq. (16) into Eq. (15) leads to

$$\dot{r}_p = z\dot{r}_z - [e\times] y\dot{\theta} - [e\times] u\dot{\psi}$$

$$[e\times] = \begin{bmatrix} 0 & -e_z & e_y \\ e_z & 0 & -e_x \\ -e_y & e_x & 0 \end{bmatrix}. \quad (17)$$

represents the screw matrix of e. This convention is adopted throughout the following formulations.

Thus, the kinematic of the moving platform can be achieved as follows

$$\omega = R_\omega \dot{\Theta} \quad (18)$$
$$\dot{r}_p = R_{rp} \dot{\Theta} \quad (19)$$

where

$$R_\omega = \begin{bmatrix} 0 & 0 & \cos\theta \\ 0 & 1 & 0 \\ 0 & 0 & -\sin\theta \end{bmatrix},$$

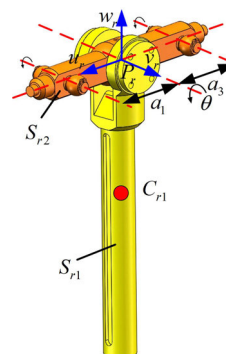$$R_{rp} = \begin{bmatrix} z & -(e\times y) & -(e\times u) \end{bmatrix}.$$

FIGURE 6. Subsystem of restricted limb.

Taking the differentiation of Eq. (18) and Eq. (19) with respect to time gives

$$\dot{\omega} = \dot{R}_\omega \dot{\Theta} + R_\omega \ddot{\Theta} \quad (20)$$
$$\ddot{r}_p = \dot{R}_{rp} \dot{\Theta} + R_{rp} \ddot{\Theta} \quad (21)$$

where

$$\dot{R}_{rp} = \begin{bmatrix} 0 & (y^\mathsf{T} e E_3 - e y^\mathsf{T}) \omega & (u^\mathsf{T} e E_3 - e u^\mathsf{T} - e^\mathsf{T} u E_3 + u e^\mathsf{T}) \omega \end{bmatrix}$$

$$\dot{R}_\omega = \begin{bmatrix} 0 & 0 & -\sin\theta \\ 0 & 0 & 0 \\ 0 & 0 & -\cos\theta \end{bmatrix}.$$

2) KINEMATICS OF RESTRICTED LIMBS

Fig. 6 illustrates the kinematic parameters of the restricted limb subsystem. It can be divided into two components according to the nature of motion, namely the restricted limb 1(S_{r1}) and the restricted limb 2(S_{r2}).

Since the restricted limb 1 only moves along the axis z, its kinematic equations can be written as follows:

$$\dot{r}_{r1} = R_{rv} \dot{\Theta} \quad (22)$$
$$\ddot{r}_{r1} = R_{rv} \ddot{\Theta} \quad (23)$$

where $\dot{r}_{r1}$ and $\ddot{r}_{r1}$ are the velocity and acceleration of point C_{r1}, respectively. R_{rv} is the transform matrix restricted limb 1, and

$$\dot{r}_{r1} = \begin{pmatrix} 0 \\ 0 \\ \dot{r}_z \end{pmatrix}, \quad \ddot{r}_{r1} = \begin{pmatrix} 0 \\ 0 \\ \ddot{r}_z \end{pmatrix}, \quad R_{rv} = \begin{bmatrix} 0 & 0 & 0 \\ 0 & 0 & 0 \\ 1 & 0 & 0 \end{bmatrix}.$$
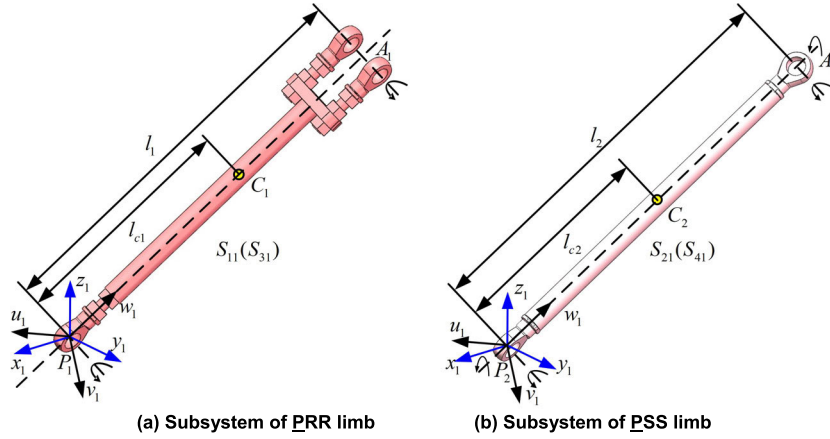
(a) Subsystem of PRR limb   **(b) Subsystem of PSS limb**

FIGURE 7. Subsystem of actuating limb.

The restricted limb 2 moves along the axis z and rotates around its mass center. Thus, its kinematic equations can be written as follows

$$\dot{r}_{r2} = R_{rv}\dot{\Theta} \tag{24}$$

$$\omega_{r2} = \dot{\theta}y = R_{r\omega}\dot{\Theta} \tag{25}$$

where $\dot{r}_{r2}$ and ω_{r2} are the velocity and angular velocity of point P_r, respectively. $R_{r\omega}$ is the transform matrix of restricted limb 2, and

$$R_{r\omega} = \begin{bmatrix} 0 & 0 & 0 \\ 0 & 1 & 0 \\ 0 & 0 & 0 \end{bmatrix}.$$

Taking the differentiation of Eq. (24) and Eq. (25) with respect to time gives

$$\ddot{r}_{r2} = R_{rv}\ddot{\Theta} \tag{26}$$

$$\dot{\omega}_{r2} = \dot{R}_{r\omega}\dot{\Theta} + R_{r\omega}\ddot{\Theta} = R_{r\omega}\ddot{\Theta} \tag{27}$$

where $\ddot{r}_{r2}$ and $\dot{\omega}_{r2}$ are the acceleration and angular acceleration of point P_r, respectively.

3) KINEMATICS OF ACTUATING LIMBS

Fig. 7 illustrates the kinematic parameters of the actuating limb subsystem.

Taking the left product of w_i on both sides of Eq. (7) gives

$$(w_i \times z)\dot{r}_z = w_i \times (\dot{q}_iz) + l_iw_i \times (\omega_i \times w_i) - w_i \times (\omega \times a_i). \tag{28}$$

The equation can be simplified as follows

$$l_i\omega_i = (w_i \times z)\dot{r}_z + \left(w_i^T a_iE_3 - a_iw_i^T\right)\omega - [w_i\times]\dot{q}_i. \tag{29}$$

Then, it can be rewritten in the matrix form

$$\omega_i = J_{\omega i}\dot{\Theta} \tag{30}$$

where

$$J_{\omega i} = J_{p\omega i} - J_{q\omega i}, \quad J_{q\omega i} = \frac{1}{l_i}[w_i\times]J_{qi}$$

$$J_{p\omega i} = \left[\frac{1}{l_i}(w_i \times z) \quad \frac{1}{l_i}\left(w_i^T a_iE_3 - a_iw_i^T\right)y \quad \frac{1}{l_i}\left(w_i^T a_iE_3 - a_iw_i^T\right)u \right]$$

$$E_3 = \begin{bmatrix} 1 & 0 & 0 \\ 0 & 1 & 0 \\ 0 & 0 & 1 \end{bmatrix}.$$

Taking the differentiation of Eq. (24) with respect to time gives

$$\dot{\omega}_i = \dot{J}_{\omega i}\dot{\Theta} + J_{\omega i}\ddot{\Theta} \tag{31}$$

where

$$\dot{J}_{\omega i} = \dot{J}_{p\omega i} - \dot{J}_{q\omega i}, \quad \dot{J}_{p\omega i} = \begin{bmatrix} \dot{J}_{p\omega i1} & \dot{J}_{p\omega i2} & \dot{J}_{p\omega i3} \end{bmatrix}$$

$$\dot{J}_{q\omega i} = \frac{1}{l_i}[(\omega_i \times w_i)\times]J_{qi} + \frac{1}{l_i}[w_i\times]\dot{J}_{qi}$$

$$\dot{J}_{p\omega i1} = \frac{1}{l_i}\left(w_iz^T - z^Tw_iE_3\right)\omega_i$$

$$\dot{J}_{p\omega i2} = \frac{1}{l_i}\begin{pmatrix} (\omega_i \times w_i)^T a_iE_3 + w_i^T(\omega \times a_i)E_3 \\ -(\omega \times a_i)w_i^T - a_i(\omega_i \times w_i)^T \end{pmatrix}y$$

$$\dot{J}_{p\omega i3} = \frac{1}{l_i}\begin{pmatrix} (\omega_i \times w_i)^T a_iE_3 + w_i^T(\omega \times a_i)E_3 \\ -(\omega \times a_i)w_i^T - a_i(\omega_i \times w_i)^T \end{pmatrix}$$

$$\times u - \frac{1}{l_i}\left(w_i^T a_iE_3 - a_iw_i^T\right)\dot{u}.$$

According to Fig. 7, the position of the driving link mass center can be expressed as

$$r_{ci} = b_i + q_iz + l_{ci}w_i \tag{32}$$

where r_{ci} and l_{ci} are the vector of OC_i and the length of P_iC_i, respectively.

Taking the differentiation of Eq. (32) with respect to time gives

$$\dot{r}_{ci} = \dot{q}_i - l_{ci}[w_i\times]\omega_i \tag{33}$$

It can be simplified as

$$\dot{r}_{ci} = J_{vi}\dot{\Theta}_i \tag{34}$$

where $\dot{r}_{ci}$ is the velocity of point C_i, and

$$J_{vi} = J_{qi} - l_{ci}[w_i\times]J_{\omega i}$$

Taking the differentiation of Eq. (34) with respect to time gives

$$\ddot{r}_{ci} = \dot{J}_{vi}\dot{\Theta}_i + J_{vi}\ddot{\Theta}_i \tag{35}$$

where $\ddot{r}_{ci}$ is the acceleration of point C_i, and

$$\dot{J}_{vi} = \dot{J}_{qi} - l_{ci}[(\omega_i \times w_i)\times]J_{\omega i} - l_{ci}[w_i\times]\dot{J}_{\omega i}.$$

B. INVERSE DYNAMIC MODEL

According to ref [34], the velocity and acceleration mapping relationship between the operating space and the joint space can be established by Jacobian matrix and Hessian matrix. The generalized velocity and generalized force of each moving component can be evaluated accordingly. Therefore, the virtual work principle is considered to be the most effective method to establish the inverse dynamic model of parallel mechanism. Before the formulation of the inverse dynamic, four assumptions are made as followed [33]: (1) neglecting the inertias of all joints; (2) assuming all limbs are axially symmetrical; (3) assuming the slider and its accessories are a lumped mass attached to each P̲ limb; (4) neglecting the friction and clearance between the slider and the spherical hinge.

The virtual work principle of each subsystem can be expressed as follows

1) VIRTUAL WORK PRINCIPLE OF PART S_{i2}

According to Newton's second law, it can be concluded that

$$F_{qi} = m_{qi}g - m_{qi}\ddot{r}_{ci} \tag{36}$$

where m_{qi} is the mass of S_{i2}.

The inertia moment of each branch chain S_{i2} about its center of mass is

$$T_{qi} = -I_{qi}\dot{\omega}_i - \omega_i \times (I_{qi}\omega_i) \tag{37}$$

where $I_{qi} = R_i I_{qi0} R_i^T$, I_{qi0} is the moment of inertia of each branch chain about the center of mass, and

$$I_{qi0} = \begin{bmatrix} I_{qxi} & & \\ & I_{qyi} & \\ & & I_{qzi} \end{bmatrix}.$$

The virtual work principle of part S_{i2} can be expressed as

$$\delta P_q = \sum_{i=1}^{4} \left(\delta\dot{r}_{ci}^T F_{qi} + \delta\omega_i^T T_{qi} \right). \tag{38}$$

2) VIRTUAL WORK PRINCIPLE OF THE PART S_{i1}

According to Newton's second law, it can be concluded that

$$F_{si} = m_{si}g - m_{si}\ddot{q}_i \tag{39}$$

where m_{si} is the mass of S_{i1}.

The virtual work principle of part S_{i1} can be expressed as

$$\delta P_s = \delta\dot{q}^T f + \sum_{i=1}^{4} \delta\dot{q}_i^T F_{si}. \tag{40}$$

3) VIRTUAL WORK PRINCIPLE OF THE RESTRICTED PART

For the restricted limbs, the sum of gravity and inertial forces of S_{r1} and S_{r2} can be expressed as follows:

$$F_{r1} = m_{r1}g - m_{r1}\ddot{r}_{r1} \tag{41}$$

$$F_{r2} = m_{r2}g - m_{r2}\ddot{r}_{r2} \tag{42}$$

where m_{r1} is the mass of S_{r1}, m_{r2} is the mass of S_{r2}.

Moment of inertia acting on the mass center of S_{r2} can be expressed as

$$T_{r2} = -I_{r2}\dot{\omega}_{r2} - \omega_{r2} \times (I_{r2}\omega_{r2}) \tag{43}$$

where I_{r2} is the moment of inertia of S_{r2} under the coordinate of $O - xyz$, and

$$I_{r2} = R_r I_{r20} R_r^T, \quad I_{r20} = \begin{bmatrix} I_{r2x} & & \\ & I_{r2y} & \\ & & I_{r2z} \end{bmatrix}.$$

The virtual work principle of the restricted part can be expressed as

$$\delta P_r = \delta\dot{r}_{r1}^T F_{r1} + \delta\dot{r}_{r2}^T F_{r2} + \delta\omega_{r2}^T T_{r2}. \tag{44}$$

4) VIRTUAL WORK PRINCIPLE OF THE MOVING PLATFORM

According to D'Alembert principle, the sum of gravity and inertial forces of moving platform can be expressed as follows:

$$F_p = m_p g - m_p \ddot{r}_p \tag{45}$$

where m_p is the mass of moving platform, g is the vector of gravity, and

$$g = \begin{pmatrix} 0 & 0 & g \end{pmatrix}^T.$$

According to Euler's equation, the moment of inertia about the center of mass acting on the moving platform can be expressed as

$$T_p = -I_p\dot{\omega} - \omega \times (I_p\omega) \tag{46}$$

where I_p is the moment inertia of the moving platform under coordination $O - xyz$, and

$$I_p = RI_{p0}R^T, \quad I_{p0} = \begin{bmatrix} I_{px} & & \\ & I_{py} & \\ & & I_{pz} \end{bmatrix}.$$

The virtual work principle of the moving platform can be expressed as

$$\delta P_p = \delta\dot{r}_p^T F + \delta\omega^T T + \delta\dot{r}_p^T F_p + \delta\omega^T T_p. \tag{47}$$

Then, the virtual work principle of this robot can be stated as

$$\delta P_s + \delta P_q + \delta P_r + \delta P_p = 0. \tag{48}$$

For the robot, we have

$$\delta\dot{q} = J\delta\dot{\Theta}, \quad \delta\dot{q}_i = J_{qi}\delta\dot{\Theta}, \quad \delta\dot{r}_{ci} = J_{vi}\delta\dot{\Theta}, \quad \delta\omega_i = J_{\omega i}\delta\dot{\Theta},$$

$$\delta\omega = R_\omega\delta\dot{\Theta},$$

$$\delta\dot{r}_{r1} = R_{rv}\delta\dot{\Theta}, \quad \delta\dot{r}_{r2} = R_{rv}\delta\dot{\Theta}, \quad \delta\omega_{r2} = R_{r\omega}\delta\dot{\Theta},$$

$$\delta\dot{r}_p = R_{rp}\delta\dot{\Theta}$$

Substituting them into Eq. (40) yields

$$\delta\dot{\Theta}^T J^T f + \delta\dot{\Theta}^T \sum_{i=1}^{4} J_{qi}^T F_{si} + \delta\dot{\Theta}^T \sum_{i=1}^{4} J_{vi}^T F_{qi}$$

$$+ \delta\dot{\Theta}^T \sum_{i=1}^{4} J_{\omega i}^T T_{qi} + \delta\dot{\Theta}^T R_{rv}^T F_{r1} + \delta\dot{\Theta}^T R_{rv}^T F_{r2}$$

$$+ \delta\dot{\Theta}^T R_{r\omega}^T T_{r2} + \delta\dot{\Theta}^T R_{rp}^T F + \delta\dot{\Theta}^T R_\omega^T T + \delta\dot{\Theta}^T R_{rp}^T F_p$$

$$+ \delta\dot{\Theta}^T R_\omega^T T_p = 0. \tag{49}$$

Since Eq. (41) is valid for any $\delta\dot{\Theta}^{\mathrm{T}}$, it follows that

$$J^{\mathrm{T}}f + \sum_{i=1}^{4} J_{qi}^{\mathrm{T}}F_{si} + \sum_{i=1}^{4} J_{vi}^{\mathrm{T}}F_{qi} + \sum_{i=1}^{4} J_{\omega i}^{\mathrm{T}}T_{qi} + R_{rv}^{\mathrm{T}}F_{r1}$$
$$+ R_{rv}^{\mathrm{T}}F_{r2} + R_{r\omega}^{\mathrm{T}}T_{r2} + R_{rp}^{\mathrm{T}}F + R_{\omega}^{\mathrm{T}}T + R_{rp}^{\mathrm{T}}F_p + R_{\omega}^{\mathrm{T}}T_p = 0 \quad (50)$$

The inverse dynamic equation of the robot based on the virtual work principle is as follows:

$$J^{\mathrm{T}}f = D(\Theta)\ddot{\Theta} + H(\Theta, \dot{\Theta})\dot{\Theta} + G(\Theta) + E(\Theta) \quad (51)$$

It can be further simplified as follows:

$$J^{\mathrm{T}}f = \Gamma \quad (52)$$

where

$$E = -\left(R_{rp}^{\mathrm{T}}F + R_{\omega}^{\mathrm{T}}T\right)$$
$$\Gamma = D(\Theta)\ddot{\Theta} + H(\Theta, \dot{\Theta})\dot{\Theta} + G(\Theta) + E(\Theta)$$

$$H = \begin{pmatrix} \sum_{i=1}^{4}\left(m_{si}J_{qi}^{\mathrm{T}}\dot{J}_{qi}\right) + \sum_{i=1}^{4}\left(m_{qi}J_{vi}^{\mathrm{T}}\dot{J}_{vi}\right) \\ + \sum_{i=1}^{4}\left(J_{\omega i}^{\mathrm{T}}I_{qi}\dot{J}_{\omega i} + J_{\omega i}^{\mathrm{T}}[\omega_i \times]I_{qi}J_{\omega i}\right) \\ + R_{r\omega}^{\mathrm{T}}[\omega_{r2} \times]I_{r2}R_{r\omega} + R_{\omega}^{\mathrm{T}}I_p\dot{R}_{\omega} \\ + R_{\omega}^{\mathrm{T}}[\omega \times]I_pR_{\omega} + m_pR_{rp}^{\mathrm{T}}\dot{R}_{rp} \end{pmatrix}$$

$$D = \begin{pmatrix} \sum_{i=1}^{4}\left(m_{si}J_{qi}^{\mathrm{T}}J_{qi}\right) + \sum_{i=1}^{4}\left(m_{qi}J_{vi}^{\mathrm{T}}J_{vi}\right) \\ + \sum_{i=1}^{4}\left(J_{\omega i}^{\mathrm{T}}I_{qi}J_{\omega i}\right) + m_pR_{rp}^{\mathrm{T}}R_{rp} + m_{r1}R_{rv}^{\mathrm{T}}R_{rv} \\ + m_{r2}R_{rv}^{\mathrm{T}}R_{rv} + R_{r\omega}^{\mathrm{T}}I_{r2}R_{r\omega} + R_{\omega}^{\mathrm{T}}I_pR_{\omega} \end{pmatrix}$$

$$G = -\begin{pmatrix} \sum_{i=1}^{4}\left(m_{si}J_{qi}^{\mathrm{T}}g\right) + \sum_{i=1}^{4}\left(m_{qi}J_{vi}^{\mathrm{T}}g\right) \\ + m_{r1}R_{rv}^{\mathrm{T}}g + m_{r2}R_{rv}^{\mathrm{T}}g + m_pR_{rp}^{\mathrm{T}}g \end{pmatrix}.$$

C. VIRTUAL PROTOTYPE VALIDATION

The dynamic simulation is carried out in ADAMS to verify the correctness of the inverse dynamic formulation before the analysis of its dynamic performance. Since the actuating forces are not unique as previously noted, the 4th limb is removed to implement the simulation. As a result, the redundant parallel mechanism degenerates into normal one. The validation process of the inverse dynamic model is shown in Fig. 8.

The moving platform trajectory's combined translation (r_z) with rotation (θ, φ) in the base reference frame is defined as

$$\begin{cases} r_z = r_0 + A\sin(2\pi ft + \pi/2) \\ \theta = \theta_{\max}\sin(2\pi ft) \\ \varphi = \varphi_{\max}\sin(2\pi ft) \end{cases} \quad (53)$$

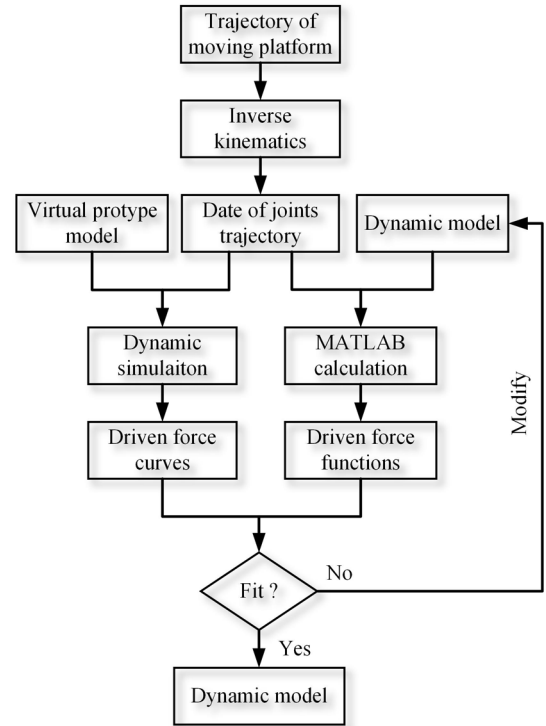$r_0 = 0.52\text{m}$, $A = 0.02\text{m}$, $\theta_{\max} = 30°$, $\varphi_{\max} = 20°$, $f = 0.4\text{Hz}$.

FIGURE 8. Validation process of inverse dynamic model.

TABLE 1. Kinematic parameters.

a_1	b_1	a_2	b_2	l_1	e
0.073 m	0.073 m	0.063 m	0.063 m	0.332 m	0.025 m
l_{c1}	l_{c2}	l_{c3}	l_{c4}	l_2	/
0.2213 m	0.16 m	0.2213 m	0.16 m	0.324 m	/

With the kinematic and dynamic parameters listed in Table 1 and Table 2, the simulation results of ADAMS and the inverse dynamic formulation are shown in Fig. 9. The red line is the result of the dynamic formulation and the blue dot line is the simulation result in ADAMS. As we can see, the simulation results are very close and the errors of the second limb are greater than the other limbs, which can be explained as follows. The mass center bias to the norm direction of the axis *v* after the fourth limb is removed is not reflected in the dynamic formulation. This result indicates that the correctness of the inverse dynamic model.

D. ACTUATING FORCE OPTIMIZATION

The solution of the inverse dynamic equation is not unique, since the Jacobi matrix is not a square matrix. Therefore, the number of the unknown quantities is larger than that of the equations of dynamics. This infinite number of possible solutions allows the actuating forces to be optimized according to the requirements. According to ref [36], the analytical relationship between the binding force of each branch of this special mechanism and the external force can be solved by Moore-Penrose generalized inverse method.

TABLE 2. Dynamic parameters.

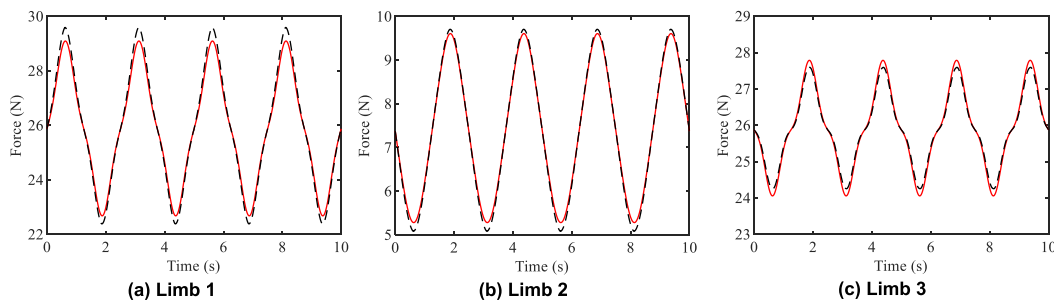| m_{s1}	m_{s2}	m_{q1}	I_{q10}	m_{q2}	I_{q20}
0.358 kg	0.282 kg	0.657 kg	diag[0.0001 0.688 0.686] kg·m²	0.470 kg	diag[0.00002 0.0044 0.0044] kg·m²
m_{r1}	g	m_{r2}	I_{r20}	m_p	I_{p0}
1.622 kg	9.8067 kg	0.506 kg	diag[0.0018 0.0018 0.000086] kg·m²	1.184 kg	diag[0.0053 0.008 0.003] kg·m²

FIGURE 9. Simulation results comparison between dynamic model and virtual prototype.
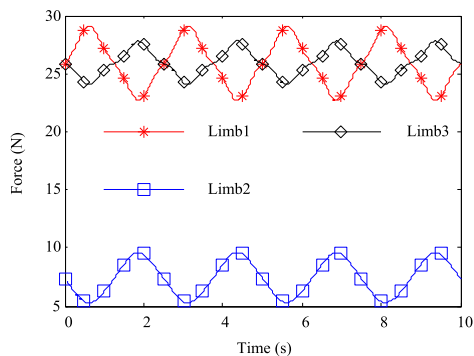

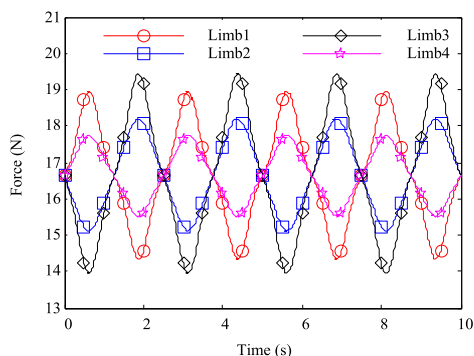**FIGURE 10.** Limb force in non-redundant condition.

FIGURE 11. Limb force in redundant condition.

Thus, the actuating force f can be further solved as follows:

$$f = J\left(J^{\mathrm{T}}J\right)^{-1}\Gamma = J^{+\mathrm{T}}\Gamma \tag{54}$$

where $J^{+\mathrm{T}}$ is the Moore-Penrose generalized inverse of Jacobian matrix J.

Fig. 10 and Fig. 11 illustrate the actuating force of each limb in non-redundant and redundant conditions, respectively. As we can see, the forces of each limb in the non-redundant condition are extremely unbalanced. The maximal force of the driving joint is 27 N, while the minimal force is only 6 N. After utilizing the weighted Moore-Penrose generalized inverse method to optimize the force of each limb, the maximal force reduces to 18.7 N; the force is much more balanced. This indicates that the actuation redundancy can improve the performance of the parallel robot compared with the non-redundant mechanism.

IV. INERTIA INDICES AND DYNAMIC PERFORMANCE ANALYSIS

In this section, two dynamic inertia indices are introduced and the dynamic performance analysis of AirGait is carried out.

A. INERTIA INDICES

The parallel robot has several limbs. This structural characteristic incurs coupling in each limb. The change of the actuating force in one limb results in the change of the velocity and acceleration in other limbs. Thus, it affects the dynamic characteristic and control accuracy of the robot. To analyze the coupling effect between different limbs, the dynamic model in the joint space is first derived.

According to Eq. (10) and Eq. (13), we can obtain

$$\dot{\Theta} = J^{+}\dot{q} \tag{55}$$

$$\ddot{\Theta} = J^{+}\ddot{q} - J^{+}\dot{J}J^{+}\dot{q}. \tag{56}$$

Substituting Eq. (55) and Eq. (56) into Eq. (51) yields

$$f = M\ddot{q} + C\dot{q} + K \tag{57}$$

where

$$M = \left(J^{+}\right)^{\mathrm{T}}D(\Theta)J^{+}$$

$$C = \left(J^{+}\right)^{\mathrm{T}}H(\Theta, \dot{\Theta})J^{+} - \left(J^{+}\right)^{\mathrm{T}}D(\Theta)J^{+}\dot{J}J^{+}$$

$$K = \left(J^{+}\right)^{\mathrm{T}}(G(\Theta) + E(\Theta)).$$

Matrix M is the inertia matrix in the joint space. The principle diagonal elements reflect the inertia properties of
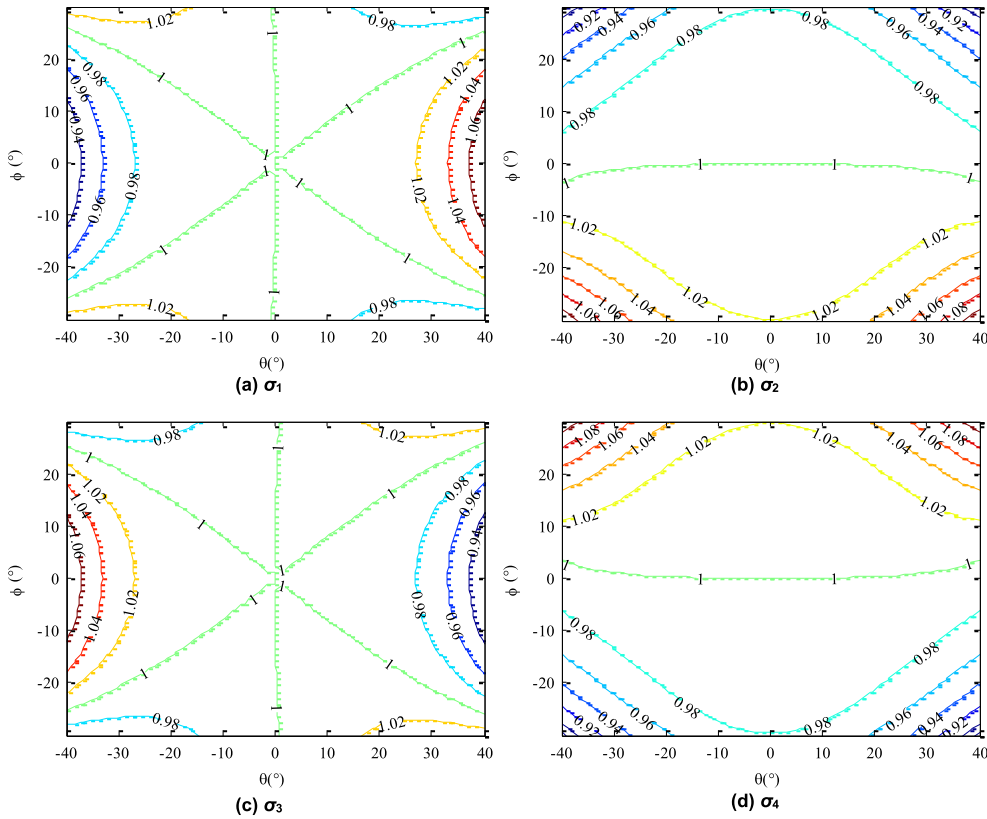
FIGURE 12. Distribution of CEON index.

the corresponding limbs, and the other elements reflect the coupling between the limbs of the parallel robot [26].

Considering in the condition of acceleration and deceleration, the terms related to acceleration and deceleration will play a leading role in the dynamic model, so the terms of velocity, gravity and external force are not considered in the dynamic index. In this paper, two indices are defined to reflect the coupling effect of the other neighboring limbs (CEON index) and the coupling effect of each neighboring limb (CEEN index). They are defined as follows.

1) CEON INDEX

This index is the ratio of the sum of absolute values of the elements except the principle diagonal element to the principle diagonal element in the *i*th row of matrix $\boldsymbol{M}$.

$$\sigma_i = \frac{\sum\limits_{j \neq i}^{n} \left| \boldsymbol{M}_{ij} \right|}{\boldsymbol{M}_{ii}} \qquad (58)$$

where *n* is the number of branches, and $n = 4$; σ_i reflects the coupling effect of other actuating limb, the value reflects the coupling strength. The increase of this index indicates the increase of coupling effect.

2) CEEN INDEX

This index is the ratio of the absolute values of the elements except the principle diagonal element to the principle diagonal element in the *i*th row of matrix $\boldsymbol{M}$.

$$\mu_{ij} = \frac{\left| \boldsymbol{M}_{ij} \right|}{\boldsymbol{M}_{ii}} \qquad (59)$$

where μ_{ij} reflects the coupling effect of the *j*th limb to the actuating limb *i*, the value reflects the coupling strength, and $j \neq i$. The increase of this index indicates an increase of the coupling effect.

It should be pointed out that the CEEN index needs to be adopted with the CEON index to carry out a comprehensive analysis on the coupling effect of parallel robot. The next section will introduce the distribution of the coupling effect among limbs based on these two indices.

B. DYNAMIC PERFORMANCE ANSLYSIS

In this section, the dynamic performance analysis is carried out by using the two dynamic indices.

1) DISTRIBUTION OF CEON INDEX

The distribution of the dynamic performance index to reflect the coupling effect of the other neighboring limbs to the dominant limb is shown in Fig. 12. Fig. 12 (a) indicates that the coupling effect is nearly constant in the range of $\theta \in [-15, 15]$ and $\phi \in [-20, 20]$, and the coupling effect smoothly changes after exceeding this range. Fig. 12 (b) indicates that the coupling effect is nearly constant in the range of $\theta \in [-10, 10]$ and $\phi \in [-10, 10]$, and the coupling effect smoothly changes after exceeding this range. Fig. 12 (c) indicates limb 3 has the same constant range as limb 1, and the changing trend is contrary to limb 1. Fig. 12 (d) indicates limb 4 has the same constant range as limb 2, and the changing trend is contrary to limb 2. These results indicate that significant coupling exists among the limbs, since the ratio of the four actuating limb is consistently
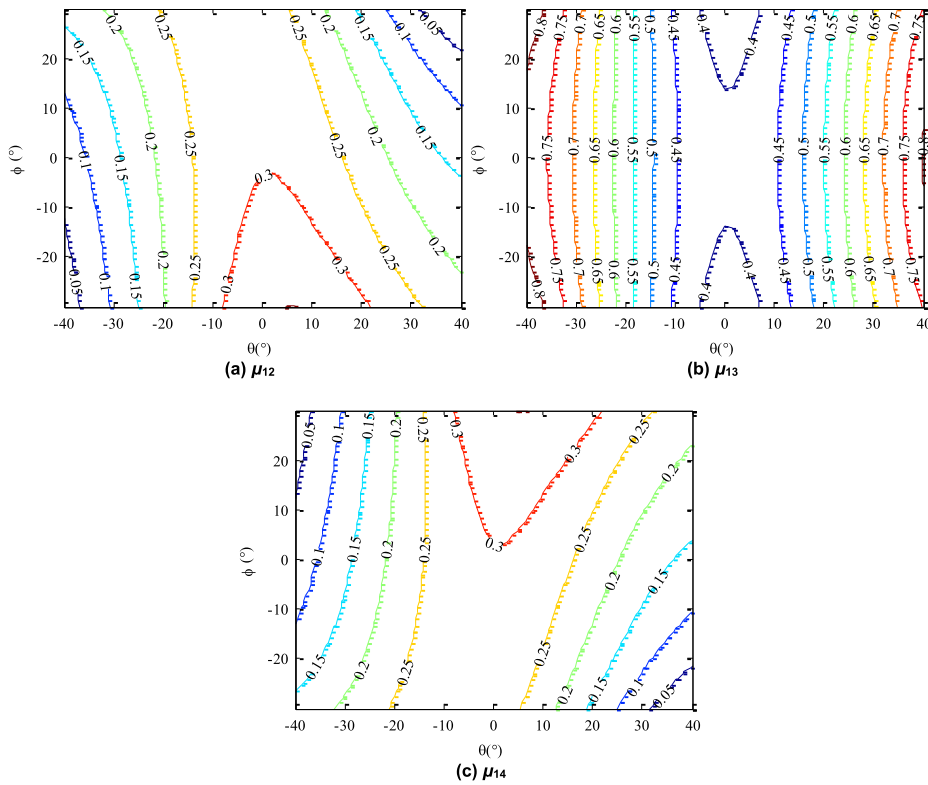
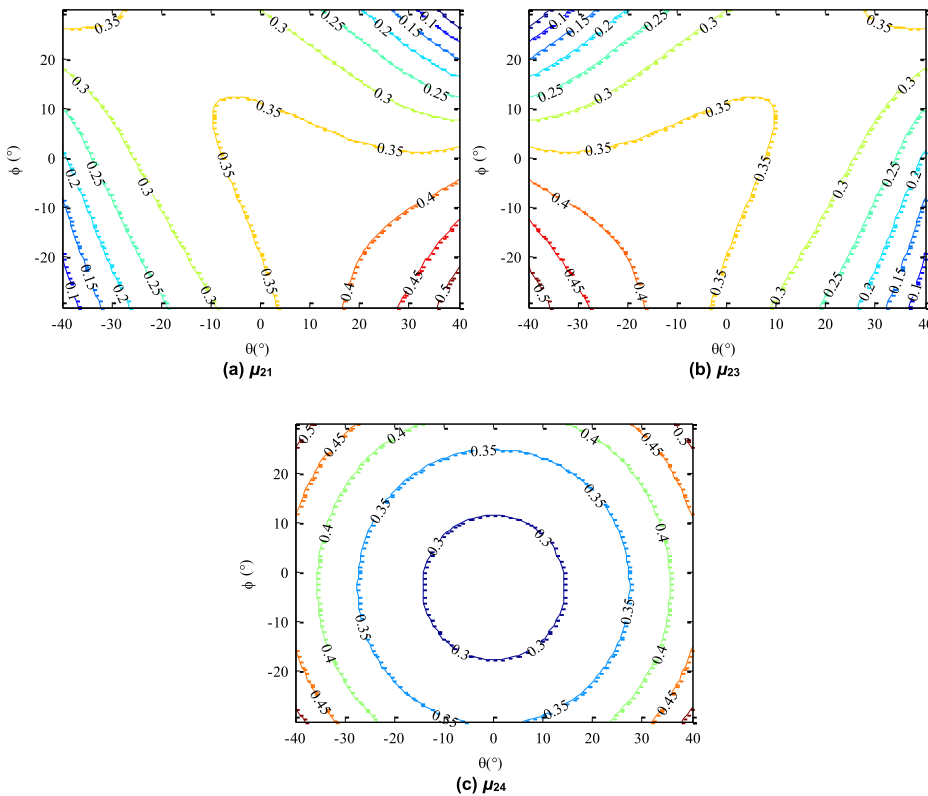**FIGURE 13.** Distribution of CEEN index for limb 1.

FIGURE 14. Distribution of CEEN index for limb 2.

near the value of 1 in the working space. Thus, the coupling effect cannot be neglected in the design of dynamic control strategies.

2) DISTRIBUTION OF CEEN INDEX

Fig. 13 illustrates the distribution of the dynamic performance index to reflect the coupling effect of each neighboring limb
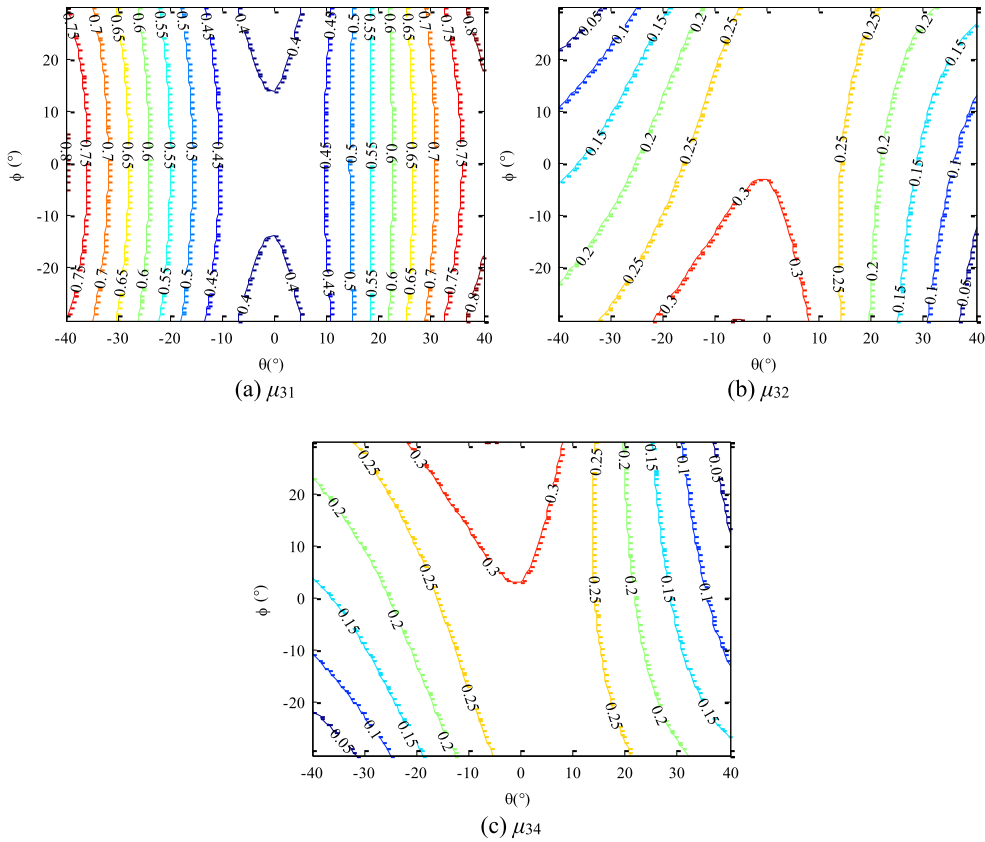
(a) μ_{31}

(b) μ_{32}

(c) μ_{34}

FIGURE 15. Distribution of CEEN index for limb 3.

to the dominant limb 1. Fig. 13 (a) illustrates that the coupling effect of limb 2 reaches the maximal value in the position of $\theta = 0$. It decreases along the direction of θ, and is constant in the direction of ϕ; Fig. 13 (b) illustrates that the coupling effect of limb 3 reaches the minimal value in the range of $\theta = 0$. It increases along the direction of θ, and is constant in the direction of ϕ. Fig. 13 (c) illustrates that the coupling effect of limb 4 reaches the maximal value in the position of $\theta = 0$. It decreases along the direction of θ, and is constant in the direction of ϕ. Fig. 13 also illustrates that the coupling effect of limb 3 exceeds those of limb 2 and limb 4.

Fig. 14 illustrates the distribution of the dynamic performance index to reflect the coupling effect of each neighboring limb to the dominant limb 2. Fig. 14 (a) illustrates that the coupling effect of limb 1 decreases along the direction of ϕ when the value of θ is greater than 0, while it increases along the direction of ϕ when the value of θ is less than 0. Fig. 14 (b) illustrates that the coupling effect of limb 3 increases along the direction of ϕ when the value of θ is greater than 0, while it decreases along the direction of ϕ when the value of θ is less than 0. Fig. 14 (c) illustrates that the coupling effect of limb 4 reaches the minimal value in the position of $\theta = 0$ and $\phi = 0$. It increases along the direction of θ and ϕ; it is symmetric around θ and ϕ. Fig. 14 also illustrates that the coupling effect of limb 4 is not more significant than that of limb 1 and limb 3.

Fig. 15 illustrates the distribution of the dynamic performance index to reflect the coupling effect of each neighboring

limb to the dominant limb 3. Fig. 15 (a) illustrates that the coupling effect of limb 1 reaches the minimal value in the range of $\theta = 0$. It increases along the direction of θ, and is constant in the direction of ϕ. Fig. 15 (b) illustrates that the coupling effect of limb 2 reaches the maximal value in the position of $\theta = 0$. It decreases along the direction of θ, and is constant in the direction of ϕ. Fig. 15 (c) illustrates that the coupling effect of limb 4 reaches the maximal value in the position of $\theta = 0$. It decreases along the direction of θ, and is constant in the direction of ϕ. Fig. 15 also illustrates that the coupling effect of limb 1 exceeds those of limb 2 and limb 4.

Fig. 16 illustrates the distribution of the dynamic performance index to reflect the coupling effect of each neighboring limb to the dominant limb 4. Fig.16 (a) illustrates that the coupling effect of limb 1 increases along the direction of ϕ when the value of θ is greater than 0, while it decreases along the direction of ϕ when the value of θ is less than 0. Fig. 16 (b) illustrates that the coupling effect of limb 2 reaches the minimal value in the position of $\theta = 0$ and $\phi = 0$. It increases along the direction of θ and ϕ; it is symmetric around θ and ϕ. Fig. 16 (c) illustrates that the coupling effect of limb 3 decreases along the direction of ϕ when the value of θ is greater than 0, while it increases along the direction of ϕ when the value of θ is less than 0. Fig. 16 also illustrates that the coupling effect of limb 2 is not more significant than those of limb 1 and limb 3.

From Fig. 13 to Fig. 16, we can see that the coupling effect is symmetric between the dominant limb and its neighboring
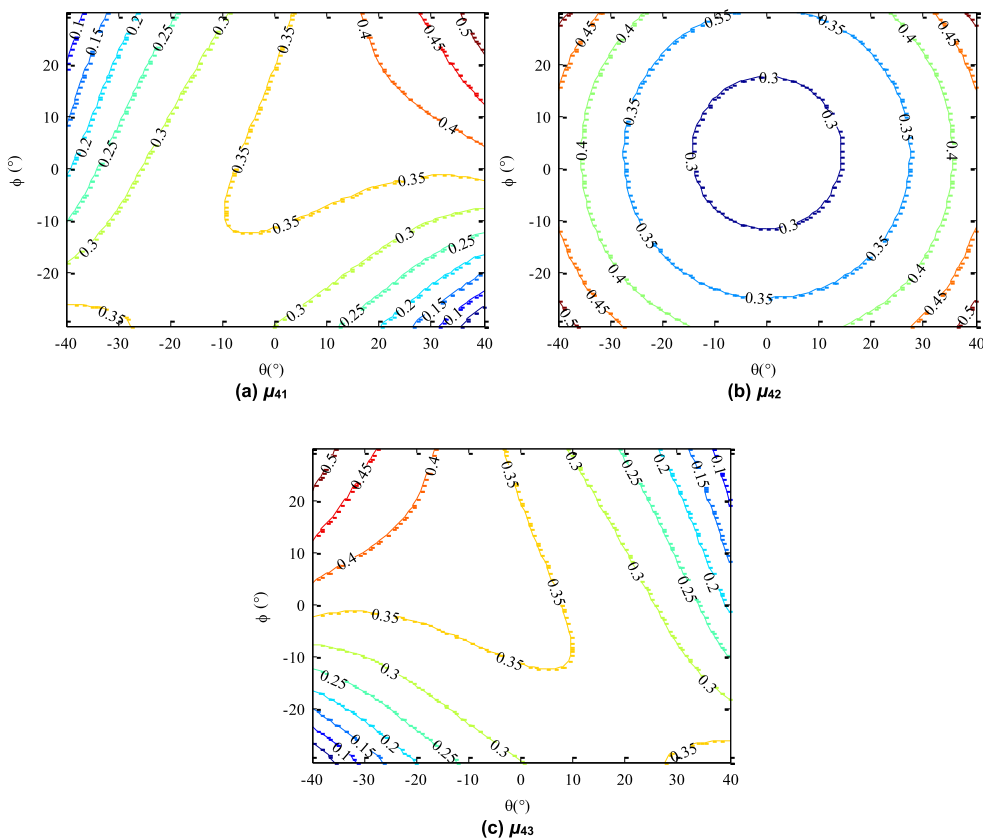
FIGURE 16. Distribution of CEEN index for limb 4.

limbs; this is caused by its symmetrical structure. These figures also indicate that the coupling property of this robot is different from the Steward parallel robot. In the Steward parallel robot, the neighboring limbs have a significant effect on the dominant limb. However, in the proposed robot, significant coupling exists between limb 1 and limb 3. In addition, the coupling of limb 1 and limb 3 to limb 2 and limb 4 is similar to the coupling that exists between limb 2 and limb 4. These coupling characteristics may be caused by its unique structure: limb 2 and limb 4 connect the moving platform with the spherical joints directly; limb 1 and limb 3 connect the restricted limb with revolution joints; and the restricted limb connects the moving platform with the revolution joints. This structure reduces the coupling between all limbs. Actually, the forward kinematics of this robot can be obtained analytically, and can be solved by a planar mechanism (i.e., only considering limb 1 and limb 3) [32].

V. CONCLUSION

This paper presents a new redundant parallel rehabilitation robot and implements an in-depth study on the coupling characteristics of it through its inverse dynamic model. The dynamic model is based on the virtual work principle and the concept of linked Jacobian matrices. The major contributions of this paper can be summarized as follows:

(1) The dynamic model of a new redundant parallel rehabilitation robot. The dynamic simulation of the non-redundant condition is implemented in ADAMS and MATLAB. The simulation results in ADAMS and MATLAB are very similar; these validate the correctness of the inverse dynamic model of the proposed redundant parallel robot.

(2) The actuating forces analysis of the new redundant parallel rehabilitation robot. The actuating forces are optimized by utilizing the weighted Moore-Penrose generalized inverse method. The optimization results indicate that the actuating force of each limb is much more balanced, and the maximal force is reduced significantly. As a result, better dynamic performance, higher stiffness, and bigger carrying capacity can be achieved.

(3) Two dynamic indices are proposed to reflect the coupling effect of the other neighboring limbs (CEON index) and the coupling effect of each neighboring limb (CEEN index). The experimental results reveal that there exists significant coupling between each actuating limb, and the coupling effect cannot be neglected in the design of dynamic control strategies. The significant coupling exists between limb 1 and limb 3. In addition, the coupling of limb 1 and limb 3 to limb 2 and limb 4 is similar to the coupling between limb 2 and limb 4.

In our future research, the CEON and CEEN indices will be employed for the dynamic workspace optimization. Besides, guidelines for control strategies based on the dynamic model will be intensively investigated in order to achieve higher performance and control accuracy. Meanwhile, the motion

equations in inverse dynamic form are presented in closed form. However, it is not suitable for numerical calculation. In our future work, the motion equations will be transformed in recursive form for the on-line control of this robot [37].

REFERENCES

[1] Y.-J. Pi, X.-Y. Wang, and X. Gu, "Synchronous tracking control of 6-DOF hydraulic parallel manipulator using cascade control method," *J. Central South Univ.*, vol. 18, no. 5, pp. 1554–1562, Oct. 2011.

[2] Y. Jiang, T.-M. Li, and L.-P. Wang, "Dynamic modeling and redundant force optimization of a 2-DOF parallel kinematic machine with kinematic redundancy," *Robot. Comput.-Integr. Manuf.*, vol. 32, pp. 1–10, Apr. 2015.

[3] P. K. Jamwal, S. Q. Xie, Y. H. Tsoi, and K. C. Aw, "Forward kinematics modelling of a parallel ankle rehabilitation robot using modified fuzzy inference," *Mechanism Mach. Theory*, vol. 45, no. 11, pp. 1537–1554, Nov. 2010.

[4] F. Xie, X. J. Liu, and J. Wang, "Performance evaluation of redundant parallel manipulators assimilating motion/force transmissibility," *Int. J. Adv. Robot. Syst.*, vol. 8, no. 5, pp. 113–124, Nov. 2011.

[5] I. Ebrahimi, J. A. Carretero, and R. Boudreau, "3-PRRR redundant planar parallel manipulator: Inverse displacement, workspace and singularity analyses," *Mechanism Mach. Theory*, vol. 42, no. 8, pp. 1007–1016, Aug. 2007.

[6] M. Alberich-Carraminana, M. Garolera, F. Thomas, and C. Torras, "Partially flagged parallel manipulators: Singularity charting and avoidance," *IEEE Trans. Robot.*, vol. 25, no. 4, pp. 771–784, Aug. 2009.

[7] S. B. Nokleby, R. Fisher, R. P. Podhorodeski, and F. Firmani, "Force capabilities of redundantly-actuated parallel manipulators," *Mechanism Mach. Theory*, vol. 40, no. 5, pp. 578–599, May 2005.

[8] H. Su, C. Yang, G. Ferrigno, and E. De Momi, "Improved human–robot collaborative control of redundant robot for teleoperated minimally invasive surgery," *IEEE Robot. Autom. Lett.*, vol. 4, no. 2, pp. 1447–1453, Apr. 2019.

[9] Z.-S. Sun, Z.-H. Guo, and W. Tang, "Design of wearable hand rehabilitation glove with soft hoop-reinforced pneumatic actuator," *J. Central South Univ.*, vol. 26, no. 1, pp. 106–119, Jan. 2019.

[10] V. Garg, S. B. Nokleby, and J. A. Carretero, "Wrench capability analysis of redundantly actuated spatial parallel manipulators," *Mechanism Mach. Theory*, vol. 44, no. 5, pp. 1070–1081, May 2009.

[11] E. Akdoğan, E. Taçgın, and M. A. Adli, "Knee rehabilitation using an intelligent robotic system," *J. Intell. Manuf.*, vol. 20, no. 2, pp. 195–202, Jan. 2009.

[12] M. H. Korayem and H. Tourajizadeh, "Maximum DLCC of spatial cable robot for a predefined trajectory within the workspace using closed loop optimal control approach," *J. Intell. Robot. Syst.*, vol. 63, no. 1, pp. 75–99, Jan. 2011.

[13] M. H. Korayem and M. Bamdad, "Dynamic load-carrying capacity of cable-suspended parallel manipulators," *Int. J. Adv. Manuf. Technol.*, vol. 44, nos. 7–8, pp. 829–840, Jan. 2009.

[14] Z. M. Bi and B. Kang, "An inverse dynamic model of over-constrained parallel kinematic machine based on Newton–Euler formulation," *J. Dyn. Syst., Meas., Control*, vol. 136, no. 4, pp. 1–9, Jul. 2014.

[15] Y. Yang, Y. Wu, and J. Pan, "Parallel dynamics computation using prefix sum operations," *IEEE Robot. Autom. Lett.*, vol. 2, no. 3, pp. 1296–1303, Jul. 2017.

[16] Y. Yun and Y. Li, "Design and analysis of a novel 6-DOF redundant actuated parallel robot with compliant hinges for high precision positioning," *Nonlinear Dyn.*, vol. 61, no. 4, pp. 829–845, Mar. 2010.

[17] Y. Zhao and F. Gao, "Inverse dynamics of the 6-DOF out-parallel manipulator by means of the principle of virtual work," *Robotica*, vol. 27, no. 2, pp. 259–268, Mar. 2009.

[18] T. D. Thanh, J. Kotlarski, B. Heimann, and T. Ortmaier, "Dynamics identification of kinematically redundant parallel robots using the direct search method," *Mechanism Mach. Theory*, vol. 52, pp. 277–295, Jun. 2012.

[19] B. Bian and L. Wang, "Design, analysis, and test of a novel 2-DOF spherical motion mechanism," *IEEE Access*, vol. 8, pp. 53561–53574, 2020.

[20] X. Chai, M. Wang, L. Xu, and W. Ye, "Dynamic modeling and analysis of a 2PRU-UPR parallel robot based on screw theory," *IEEE Access*, vol. 8, pp. 78868–78878, 2020.

[21] A. M. Shafei and H. R. Shafei, "Considering link flexibility in the dynamic synthesis of closed-loop mechanisms: A general approach," *J. Vib. Acoust.*, vol. 142, no. 2, pp. 1–12, Apr. 2020.

[22] J. Gallardo, J. M. Rico, A. Frisoli, D. Checcacci, and M. Bergamasco, "Dynamics of parallel manipulators by means of screw theory," *Mechanism Mach. Theory*, vol. 38, no. 11, pp. 1113–1131, Nov. 2003.

[23] A. Sokolov and P. Xirouchakis, "Dynamics analysis of a 3-DOF parallel manipulator with R–P–S joint structure," *Mechanism Mach. Theory*, vol. 42, no. 5, pp. 541–557, May 2007.

[24] X. L. Chen, X. X. Liang, Y. Deng, and Q. Wang, "Rigid dynamic model and analysis of 5-DOF parallel mechanism," *Int. J. Adv. Robot. Syst.*, vol. 12, no. 7, pp. 1–9, Jul. 2015.

[25] H. Zuo and G.-L. Tao, "Cross-coupling integral adaptive robust posture control of a pneumatic parallel platform," *J. Central South Univ.*, vol. 23, no. 8, pp. 2036–2047, Oct. 2016.

[26] J. Mo, Z.-F. Shao, L. Guan, F. Xie, and X. Tang, "Dynamic performance analysis of the x4 high-speed pick-and-place parallel robot," *Robot. Comput.-Integr. Manuf.*, vol. 46, pp. 48–57, Aug. 2017.

[27] Y. Yao, S. Fu, and L. Han, "Block diagonal dominance analysis and judgement of stewart platform's joint-space inertia matrix," *Chin. J. Mech. Eng.*, vol. 44, no. 6, pp. 101–106, Jan. 2008.

[28] P. Ogbobe, J. Hongzhou, H. Jingfeng, Y. Chifu, and H. Junwei, "Analysis of coupling effects on hydraulic controlled 6 degrees of freedom parallel manipulator using joint space inverse mass matrix," in *Proc. 2nd Int. Conf. Intell. Comput. Technol. Automat.*, Changsha, China, Oct. 2009, pp. 845–848.

[29] D. Wang, J. Wu, L. P. Wang, and X. J. Liu, "Research on the inertia coupling property of a 3-PRS parallel robot," *Chin. J. Theor. Appl. Mech.*, vol. 48, no. 4, pp. 804–812, Apr. 2016.

[30] Z.-F. Shao, X. Tang, X. Chen, and L.-P. Wang, "Research on the inertia matching of the stewart parallel manipulator," *Robot. Comput.-Integr. Manuf.*, vol. 28, no. 6, pp. 649–659, Dec. 2012.

[31] Y. Zhao and F. Gao, "Dynamic formulation and performance evaluation of the redundant parallel manipulator," *Robot. Comput.-Integr. Manuf.*, vol. 25, nos. 4–5, pp. 770–781, Aug. 2009.

[32] Y. Zhao and F. Gao, "Dynamic performance comparison of the 8PSS redundant parallel manipulator and its non-redundant counterpart—The 6PSS parallel manipulator," *Mechanism Mach. Theory*, vol. 44, no. 5, pp. 991–1008, May 2009.

[33] M. Li, T. Huang, J. Mei, X. Zhao, D. G. Chetwynd, and S. J. Hu, "Dynamic formulation and performance comparison of the 3-DOF modules of two reconfigurable PKM—The tricept and the TriVariant," *J. Mech. Des.*, vol. 127, no. 6, pp. 1129–1136, Nov. 2005.

[34] L.-W. Tsai, "Solving the inverse dynamics of a stewart-gough manipulator by the principle of virtual work," *J. Mech. Des.*, vol. 122, no. 1, pp. 3–9, Mar. 2000.

[35] S. Xie, G. Ren, J. Xiong, and Y. Lu, "A trajectory tracking control of a robot actuated with pneumatic artificial muscles based on hysteresis compensation," *IEEE Access*, vol. 8, pp. 80964–80977, 2020.

[36] Z. Wang, J. Yao, Y. Xu, and Y. Zhao, "Hyperstatic analysis of a fully prestressed six-axis force/torque sensor," *Mechanism Mach. Theory*, vol. 57, pp. 84–94, Nov. 2012.

[37] M. Korayem, A. Shafei, M. Doosthoseini, F. Absalan, and B. Kadkhodaei, "Theoretical and experimental investigation of viscoelastic serial robotic manipulators with motors at the joints using timoshenko beam theory and Gibbs–Appell formulation," *Proc. Inst. Mech. Eng., K, J. Multi-Body Dyn.*, vol. 230, no. 1, pp. 37–51, Mar. 2016.

SHENGLONG XIE was born in Anqing, China, in 1988. He received the B.S. degree in mechanical design, manufacturing and automation and the M.S. degree in mechatronic engineering from the Anhui University of Technology, Ma'anshan, China, in 2011 and 2014, respectively, and the Ph.D. degree in mechanical engineering from Tianjin University, Tianjin, China, in 2018. He is currently a Lecturer with the School of Mechanical and Electrical Engineering, China Jiliang University. His research interests include motion control of rehabilitation and industrial robots, and modeling and control of pneumatic muscle actuators with hysteresis.

KAIMING HU was born in Hangzhou, China, in 1985. He received the B.S. degree in flight vehicle design and engineering and the M.S. and Ph.D. degrees in flight vehicle design from Northwestern Polytechnical University, Xi'an, China, in 2008, 2011, and 2016, respectively. He is currently a Lecturer with the School of Mechanical and Electrical Engineering, China Jiliang University. His research interests include large deformation piezoelectric actuators, morphing wings, and active vibration control.

YANJIAN WAN was born in Gushi, China, in 1986. He received the B.S. degree in agricultural mechanization and automation from Henan Agricultural University, Zhengzhou, China, in 2009, and the Ph.D. degree in mechanical engineering from Sichuan University, Tianjin, China, in 2014. He is currently a Lecturer with the School of Mechanical and Electrical Engineering, China Jiliang University. His research interests include theory and method of innovative design of mechanical and electrical products, motion control of rehabilitation, and industrial robots.

• • •

HAITAO LIU (Member, IEEE) was born in Heilongjiang, China, in 1981. He received the B.S., M.S., and Ph.D. degrees in mechanical engineering from Tianjin University, Tianjin, China, in 2004, 2007, and 2010, respectively. He is currently a Professor with the School of Mechanical Engineering, Tianjin University. His research interests include mechanism and robotics, industrial robots, and intelligent manufacturing.